Key Points:

- The latent heat transport of the monsoon increases through the Eocene higher CO_2 concentration, but it is reduced by the Eocene topography
- The poleward heat transport of midlatitude cyclones is higher in the Northern Hemisphere in the Eocene, due to the different topography
- The Eocene northern Hadley cell circulates more heat, than in the present, while its net poleward heat transport is even less than today

Correspondence to:
F. D. Kelemen,
kelemen@iau.uni-frankfurt.de

Meridional Heat Transport in the DeepMIP Eocene Ensemble: Non-CO2 and CO2 Effects

Fanni Dora Kelemen[1], Sebastian Steinig[2], Agatha de Boer[3], Jiang Zhu[4], Wing-Le Chan[5,6], Igor Niezgodzki[7,8], David K. Hutchinson[9], Gregor Knorr[8], Ayako Abe-Ouchi[5], and Bodo Ahrens[1]

[1]Institute for Atmospheric and Environmental Sciences, Goethe University Frankfurt, Frankfurt am Main, Germany, [2]School of Geographical Sciences, University of Bristol, Bristol, UK, [3]Department of Geological Sciences, Bolin Centre for Climate Research, Stockholm University, Stockholm, Sweden, [4]Climate and Global Dynamics Laboratory, National Center for Atmospheric Research, Boulder, CO, USA, [5]AORI, The University of Tokyo, Kashiwa, Japan, [6]Research Center for Environmental Modeling and Application, JAMSTEC, Yokohama, Japan, [7]ING PAN—Institute of Geological Sciences Polish Academy of Sciences, Research Center in Kraków, Biogeosystem Modelling Group, Kraków, Poland, [8]Alfred Wegener Institute, Helmholtz Centre for Polar and Marine Research, Bremerhaven, Germany, [9]Climate Change Research Centre, University of New South Wales Sydney, Sydney, NSW, Australia

Abstract The total meridional heat transport (MHT) is relatively stable across different climates. Nevertheless, the strength of individual processes contributing to the total transport are not stable. Here we investigate the MHT and its main components especially in the atmosphere, in five coupled climate model simulations from the Deep-Time Model Intercomparison Project (DeepMIP). These simulations target the early Eocene climatic optimum, a geological time period with high CO_2 concentrations, analog to the upper range of end-of-century CO_2 projections. Preindustrial and early Eocene simulations, at a range of CO_2 levels are used to quantify the MHT changes in response to both CO_2 and non-CO_2 related forcings. We found that atmospheric poleward heat transport increases with CO_2, while oceanic poleward heat transport decreases. The non-CO_2 boundary conditions cause more MHT toward the South Pole, mainly through an increase in the southward oceanic heat transport. The changes in paleogeography increase the heat transport via transient eddies at the northern mid-latitudes in the Eocene. The Eocene Hadley cells do not transport more heat poleward, but due to the warmer atmosphere, especially the northern cell, circulate more heat in the tropics, than today. The monsoon systems' poleward latent heat transport increases with rising CO_2 concentrations, but this change is counterweighted by the globally smaller Eocene monsoon area. Our results show that the changes in the monsoon systems' latent heat transport is a robust feature of CO_2 warming, which is in line with the currently observed precipitation increase of present day monsoon systems.

Plain Language Summary In the Earth's climate system both the atmosphere and the ocean are transporting heat through different processes from the tropics toward the poles. We investigate the transport of the atmosphere in several climate model set ups, which aim to simulate the very warm climate of the early Eocene (∼56–48 Myr ago). This period is relevant, because the atmospheric CO_2 concentration was close to our pessimistic projection of CO_2 concentration for the end of the century. In our study we separate the results into transport changes due to the different set up of the Eocene, and transport changes due to larger CO_2 concentration values. We found that with rising CO_2 values the atmosphere transports more heat from the tropics to the poles. The different location of the continents and seas is influencing the heat transport of the midlatitude cyclones. The Eocene tropical meridional overturning circulation's poleward heat transport does not increase, but it circulates more heat than today. The monsoon systems seem to be affecting a globally smaller area in the Eocene, but they are also more effective in transporting heat. This conclusion is in line with the observation, that current day monsoon systems' precipitation increases, as our CO_2 concentration rises.

1. Introduction

The meridional temperature gradient is the main driving force of the atmospheric and oceanic general circulation. It is caused by differential radiative heating and leads to meridional heat transport (MHT) from the tropics to the mid- and high latitudes. It has been shown that the MHT is stable in different climate states (Krapp & Jungclaus, 2011; Smith et al., 2006; Yang et al., 2015). Bjerknes (1964) proposed that if the net radiation forcing

Writing – original draft: Fanni Dora Kelemen
Writing – review & editing: Fanni Dora Kelemen, Sebastian Steinig, Agatha de Boer, Jiang Zhu, Wing-Le Chan, Igor Niezgodzki, Gregor Knorr, Bodo Ahrens

at the top of the atmosphere (TOA) and the ocean heat storage do not vary too much, then the MHT shall be also relatively stable. This leads to the expectation that any large variations in heat transport in the atmosphere and in the ocean should be equal in magnitude and opposite in sign, nevertheless it does not rule out large changes in both ocean and atmosphere. This mechanism is known as the Bjerknes compensation (BJC). Stone (1978) later showed that the MHT is mainly determined by the solar constant, the axial tilt, the radius of the Earth and the mean planetary albedo. Among these variables only the albedo is an internal parameter of the atmosphere-ocean system, and it highly depends on temperature, as a defining factor on clouds, ice and snow. Different modeling studies suggest that the BJC is valid in different paleo climate states, for example, during the glacial-interglacial period of the last 22,000 years (Yang et al., 2015), or in the warm climate of the Middle Miocene (Krapp & Jungclaus, 2011). Also, it was found in preindustrial and in historical simulations of CMIP5 models, which is interesting because in the latter, the climate is not in equilibrium (Outten et al., 2018). Even in extreme theoretical cases, such as the aqua-planet, BJC is shown to be valid (Smith et al., 2006).

Even though total MHT is stable in different climate states, the contributions from various transport processes might change. Quantifying transport processes is a great tool to identify the large scale features of different climate states and reveal any compensating mechanism. In the climate system the heat is transported by the atmosphere and the ocean via different mechanisms. In the tropical belt both the atmosphere and the ocean contribute to the MHT equally, while at higher latitudes the atmospheric transport dominates (Masuda, 1988). At lower latitudes the heat is transported mainly by the meridional overturning circulation (MOC), which is represented by the Hadley cell in the atmosphere and by the wind-driven gyres in the upper ∼1,000 m of the ocean (Held, 2001). Note that we do not evaluate separately the role of the ocean's MOC so hereafter MOC refers to the atmosphere in this study. At higher latitudes the heat is transported dominantly by the atmosphere via different eddies, such as transient eddies (TE), comprised mainly of mid-latitude cyclones, and stationary eddies (SE), which represent monsoons in the subtropics and planetary waves in midlatitudes. The stationary planetary waves are connected to varying topography and land-sea thermal contrast (Wills et al., 2019).

Change in the different transport processes have been shown to be relevant in the present climate, for example, the changes in the poleward atmospheric and oceanic heat transport has been shown to contribute to the polar amplification (Forster et al., 2021). In a warmer climate the equator-to-pole gradient of atmospheric moisture is expected to increase due to the exponentially increasing water holding capacity of warmer air. The larger moisture gradient enhances the poleward latent heat transport. This process plays an important role in polar amplification. The polar amplification on the other hand results in a weakening of the equator-to-pole temperature gradient, which decreases the dry-static energy transport, what in turn partly compensates the increase in latent heat transport (Forster et al., 2021). The latest IPCC report shows that in our current warming climate large scale circulation patterns such as the Hadley cell or the monsoon systems have been changing (Gulev et al., 2021). Regarding the Hadley circulation, studies based on reanalysis data mostly indicate changes in the northern Hadley cell, in the form of widening and strengthening of the circulation (Gulev et al., 2021). Nevertheless, under CO_2 forcing, climate models predict a larger extension in the Southern Hadley cell (Watt-Meyer et al., 2019). The North Hemisphere summer monsoon precipitation shows an increase in the recent past (Gulev et al., 2021) and future projections also predict an increase in global monsoon precipitation (Lee et al., 2021).

Investigating the large scale circulation through, the transport processes in a past warm period of Earth's climate system, can help to better understand our future in a warmer climate. Paleoclimate model simulations in contrast to future projections, have the advantage, that there are proxy data available, which help to validate the model's response to changes in the forcings. Proxies help to reduce the uncertainties of modeling a climate state in extreme circumstances. One of the best examples of past warm periods is the early Eocene climatic optimum (EECO, ∼56–48 Myr ago). It is the period of greatest sustained (>1 Myr) warmth in the last 65 million years (Lunt et al., 2017), when CO_2 concentrations are estimated to have fallen between 1,170 and 2,490 ppm (Anagnostou et al., 2020) and the estimated global mean surface temperatures reached 27.0°C (23.2–29.7°C), approximately 10–16°C warmer than preindustrial climate (Inglis et al., 2020). It has been shown (Evans et al., 2018), that the meridional temperature gradient was much weaker in the Eocene's warm climate than at present, thus indicating strong polar amplification, which is a challenge to capture for most climate models. There has been a community effort in creating a framework for the intermodel comparison of Paleocene-Eocene simulations (Lunt et al., 2017) and also to coordinate the methodology of a proxy data compilation focusing on temperature and CO_2 concentrations from this period (Hollis et al., 2019). This coordinated effort is the Deep Time Model Intercomparison Project (DeepMIP), and the time intervals it focuses on are the latest Paleocene (pre-PETM), Paleocene–Eocene

thermal maximum (PETM) and EECO. In DeepMIP, the atmospheric CO_2 concentrations and other boundary conditions, such as the paleogeography, orbital configurations, solar constant, vegetation, and lack of continental ice sheets were uniformly defined. Eight modeling groups participated in performing paleo simulations with the agreed boundary conditions. Some models are closer to the proxy records than others, but all simulations indicate a warmer than present day global mean temperature, and a smaller than present day meridional SST gradient. The Community Earth System Model (CESM), the Geophysical Fluid Dynamics Laboratory (GFDL) model and the Norwegian Earth System Model (NorESM) perform well in simulating the global mean temperature and meridional SST gradient at CO_2 levels, which are also in the proxy indicated range (Lunt et al., 2021). The closest agreement with proxy data is found for simulations at 6× times the preindustrial CO_2 concentration, which also aligns with the best-estimate of CO_2 concentration from proxy data. In terms of simulating the lowest meridional temperature gradient the most successful simulation is from CESM (Lunt et al., 2021).

Several studies have investigated the EECO's heat transport with the intention to explain its low temperature gradient. Increased heat transport, especially increased ocean transport has been suggested to be the mechanism responsible for the low meridional gradient (Barron, 1987; Sloan et al., 1995). It has been estimated that 30% or even greater increase in poleward heat transport than at present, is needed to achieve the low temperature gradient of Eocene (Huber & Nof, 2006; Sloan et al., 1995). This is problematic, since we do not know any acceptable mechanism to realize such a large transport change. The Eocene MHT have been studied with coupled global circulation models (Heinemann et al., 2009; Huber & Sloan, 2001), and they found that it is unlikely that the increased oceanic heat transport is the responsible mechanism for the low meridional temperature gradient.

In our work we focus on the changes in the different atmospheric transport processes in the EECO, to better understand the atmospheric large scale circulation pattern of this warm climate. Moreover, we separate these changes depending on their underlying causes, namely if they are driven by the CO_2 increase or the non-CO_2 forcing of the paleo simulations. We compare the results of five different models from the DeepMIP ensemble. Dividing the changes into non-CO_2 and CO_2 forcing helps us to also assess the relevance of the results for future climate scenarios, where the CO_2-driven processes become more relevant than any changes in topography. Our study aims to answer the following questions:

- Can the DeepMIP model ensemble capture the characteristics of transport processes in the preindustrial control (PI) simulations?
- What are the impacts of changes of non-CO_2 constraints (paleogeography, vegetation, no continental ice sheet) on the different atmospheric energy transport processes?
- What are the impacts of CO_2 concentration increase on the atmospheric transport processes in the 3× and 6 × CO_2 EECO simulations?
- What is the overall change (non-CO_2 and CO_2 constraints) between the PI and EECO simulations look like? Which physical transport processes are affected the most?

The paper is structured as follows, in Section 2 we briefly introduce the DeepMIP experimental design, the selected models and reanalysis, and we explain the methods used in the analysis. Then, the results section shows the transport changes due to the non-CO_2 and the CO_2 constraints, first individually and then their combined effect on changes between past and present climates. Section 4 discusses the three large scale circulation patterns, which are affected by the CO_2 and non-CO_2 constraints. In Section 5 we summarize our findings and conclude.

2. Data and Methods

In this study we analyze climate model simulations from DeepMIP simulations. We further include present day data from the ERA5 reanalysis to compare it with the respective preindustrial simulations of the DeepMIP models.

2.1. Experimental Design

The experimental design and the different models included in DeepMIP are described in Lunt et al. (2017, 2021), here we only introduce them briefly. DeepMIP was conducted to offer a consistent framework for climate model simulations of three warm periods in the latest Paleocene and early Eocene (∼55 to ∼50 Ma), which are the EECO, the PETM and the period just before the PETM (pre-PETM). These time periods of Earth's climate are

Table 1
List of Models Used in This Study From the DeepMIP Ensemble

Model (short name)	Experiments	Length of simulations (years)	Atmospheric resolutions (lat × lon)
CESM (CESM1.2_CAM5)	piControl	2,000	1.9° × 2.5°
	1×, 3×, 6×		
COSMOS (COSMOS-landveg_r2413)	piControl	9,500	3.75° × 3.75°
	1×, 3×		
GFDL (GFDL_CM2.1)	piControl	6,000	3° × 3.75°
	1×, 3×, 6×		
HadCM3 (HadCM3B_M2.1aN)	piControl	7,800	3.75° × 2.5°
	1×, 3×		
MIROC (MIROC4m)	piControl	5,000	2.79° × 2.81°
	1×, 3×		

characterized by high atmospheric CO_2 concentrations estimated to be between 800 and 3,160 ppm (Anagnostou et al., 2020), which falls in the range of 3× to 12× higher concentrations than the preindustrial value (280 ppm). The concentrations during the EECO, which is the longest of the three, is estimated to fall between 1,170 and 2,490 ppm. This is around 4× and 9× the preindustrial concentration level. Many DeepMIP groups performed multiple experiments at various CO_2 levels, for example, at 1×, 3×, 6×, or 9× the preindustrial CO_2 concentration, to capture this uncertainty. Apart from the atmospheric CO_2 concentrations other boundary conditions, such as the paleogeography, orbital configurations, solar constant, vegetation, continental ice sheets and aerosols, are needed to set up a deep-time simulation. The paleogeography used here, represents the Ypresian stage of the Eocene, where the most notable differences to today's geography are the lack of the Himalaya, the lack of the enclosed Mediterranean basin, the proto-Paratethys and the Siberian Sea and a narrower Atlantic basin. The digital reconstruction from Herold et al. (2014) is used for the paleogeography, vegetation, and river routing. The orbital configuration is set to the modern values, because it represents a forcing close to the long-term average (Lunt et al., 2017). Both the solar constant, and non-CO_2 greenhouse gas concentrations are set to preindustrial values, to find a middle ground between the uncertainty on the increased radiative forcing associated with enhanced non-CO_2 greenhouse gases and the decrease in radiative forcing via a reduced solar constant (Lunt et al., 2017). One additional important initial constraint is that there are no continental ice sheets in the Eocene simulations. Initial condition for ocean temperature and salinity are given in Lunt et al. (2017), but each modeling group followed their individual approach based on their previous paleo simulations or experiences with model instabilities.

To accept a model simulation as the representation of the paleoclimate of EECO, PETM, or pre-PETM it needs to be in (or close to) equilibrium. To assure this, three criteria are defined, the first is regarding the length of the simulation (more than 1,000 years) the second considers the energy balance of the models (less than 0.3 W m^{-2} net radiation imbalance at the TOA or similar imbalance to that of the PI), and last is the test if the ocean has reached its equilibrium state (sea-surface temperature trend is less than 0.1°C per century in the global mean). These latter two shall be based on the final 100 years of the simulation. Most of the simulations fulfill these conditions, and those which are not, only overstep the thresholds slightly, thus Lunt et al. (2021) concluded them to be sufficiently equilibrated.

2.2. Models

In total 8 models participated in DeepMIP from which we selected 5, depending on the available experiment types. In our study we focus on the CO_2 and non-CO_2 effects, thus we needed from all models a PI simulation, a $1 \times CO_2$ Eocene simulation, and also at least one Eocene simulation with a higher CO_2 concentration. The three models, which we did not include in our study (INMCM, IPSL, NorESM), are left out because there was no available $1 \times CO_2$ simulation. We have chosen 3× and $6 \times CO_2$ concentration simulations, where they were available (see Table 1). These concentrations, represent the pre-PETM and the EECO/PETM conditions respectively. All models are coupled ocean-atmosphere models. The selected simulations are summarized in Table 1. An overview

of each model is listed below, while the more elaborate description of the simulations and models are found in Lunt et al. (2021) and in the corresponding papers.

CESM stands for the Community Earth System Model version 1.2, it consists of the Community Atmosphere Model 5.3 (CAM), the Community Land Model 4.0 (CLM), the Parallel Ocean Program 2 (POP), the Los Alamos sea ice model 4 (CICE), the River Transport Model, and a coupler connecting them (Hurrell et al., 2013). The atmospheric part of the coupled system has 30 hybrid sigma-pressure levels and a horizontal resolution of $1.9° \times 2.5°$ (latitude $\times$ longitude). The ocean and sea ice model use a nominal $1° \times 1°$ displaced pole Greenland grid with 60 vertical levels in the ocean. Some modifications were needed to make the Earth system model applicable for a paleoclimate simulation with a high CO_2 level applicable. These effected the radiation parametrization, and the marginal sea balancing scheme. The ocean was initialized from a previous PETM simulation (Kiehl & Shields, 2013) without any sea ice. The simulations have been integrated for 2000 model years, except the $1 \times CO_2$ simulation, which has been integrated for 2600 model years.

COSMOS is developed at the Max Planck Institute for Meteorology and uses the atmospheric general circulation model ECHAM5 (Roeckner et al., 2003) and the Max-Planck-Institute for Meteorology Ocean Model (MPIOM) (Marsland et al., 2003) for the ocean and sea ice components. The atmospheric part has 19 vertical hybrid sigma-pressure levels and a horizontal resolution approximately $3.75° \times 3.75°$. The ocean and sea ice dynamics are calculated on a bipolar curvilinear model grid with formal resolution of $3.0° \times 1.8°$ (longitude $\times$ latitude) and 40 unequal vertical levels. COSMOS' performance in paleoclimate studies is described in Stepanek and Lohmann (2012). The ocean was initialized with uniformly horizontal and vertical temperatures of 10°C in the $3 \times CO_2$ concentration simulation and then the simulations with $1 \times$ and $4 \times CO_2$ concentrations were restarted from $3 \times CO_2$ after 1,000 years. The simulations were started with transient orbital configurations and were run to model year 8000, then they were run with preindustrial orbital parameters for the last 1,500 years.

GFDL means the Geophysical Fluid Dynamics Laboratory (GFDL) CM2.1 model (Delworth et al., 2006), with modifications to the late Eocene (Hutchinson et al., 2018, 2019). The CM2.1 consists of Atmosphere Model 2, Land Model 2, the Sea Ice Simulator 1. The ocean is calculated by the modular ocean model version 5.1.0. The atmosphere has 24 vertical levels and a horizontal resolution of $3° \times 3.75°$. The ocean and sea ice components are calculated over 50 vertical levels with the horizontal resolution of $1° \times 1.5°$ (latitude $\times$ longitude), and a tripolar grid is used as in Hutchinson et al. (2018). Due to the paleogeography some manual adjustments were made in the ocean grid. The ocean temperature was initiated from idealized conditions, similar to those outlined in Lunt et al. (2017). The simulations were run for a total of 6,000 years. During the initial 2,000 years, two adjustments were performed on the ocean temperature to accelerate the approach to equilibrium. This approach led to instabilities at $6 \times CO_2$ level, this simulation was instead initialized using a globally uniform temperature of 19.32°C and was run continuously for 6,000 years.

HadCM3 is the abbreviation of the Hadley Center Climate Model (Valdes et al., 2017). The atmosphere has 19 vertical levels and a horizontal resolution of $3.7° \times 2.5°$, while the ocean is calculated on a $1.25° \times 1.25°$ grid over 20 vertical levels. A few changes were necessary to adapt the model to the deep-time simulations, such as a salinity flux correction, prognostic 1D ozone scheme instead the fixed vertical profile, and also the disabling of modern-day specific parametrizations, for example, in the Mediterranean and the Hudson Bay. The ocean was initialized from the final state of Eocene model simulations using lower resolution in the ocean, HadCM3L. The HadCM3L simulations were initialized from a similar idealized temperature and salinity state as described in Lunt et al. (2017). HadCM3 simulations were started from the respective HadCM3L integrations after 4,400–4,900 years of spin up and run for a further 2,950 years.

MIROC stands for Model for Interdisciplinary Research on Climate (Chan & Abe-Ouchi, 2020). The land surface model is the Minimal Advanced Treatments of Surface Interaction and Runoff (MATSIRO) (Takata et al., 2003). The ocean component is the version 3.4 of the CCSR (Center for Climate System Research) Ocean Component Model (COCO) (Hasumi, 2000). The atmosphere has 20 vertical sigma levels and a horizontal resolution of approximately $2.79° \times 2.81°$ (latitude x longitude). The ocean has 44 levels and a horizontal resolution is set to 256×196 (longitude $\times$ latitude), with a higher resolution in the tropics. The atmosphere is initialized from a previous experiment without ice sheets and with a $\times 2$ CO_2 concentration. The ocean is initialized based on previous MIROC paleoclimate experiments and on the recommendations from Lunt et al. (2017). For the experiments the model was run for 5000 model years.

2.3. Reanalysis

We use the atmospheric reanalysis ERA5 (Hersbach et al., 2020) to evaluate the DeepMIP ensembles performance for the PI simulation. ERA5 is a comprehensive reanalysis from Copernicus Climate Change Service (C3S) produced by ECMWF and it is based on the Integrated Forecasting System Cy41r2 which was operational in 2016. In our study we use monthly averaged data on pressure levels and on single levels (H. Hersbach et al., 2019a, 2019b) from the time period 1991–2020 on a horizontal resolution of approximately $0.25° \times 0.25°$.

2.4. Partitioning the Meridional Heat Transport

In our study we analyze the total MHT, and focus on its components, in the atmosphere. We follow the method described in Donohoe et al. (2020). First the MHT is partitioned between the ocean and the atmosphere

$$MHT = OHT + AHT, \tag{1}$$

and the atmospheric transport is further partitioned into contributions from MOC, SE, and TE

$$AHT = MOC + SE + TE. \tag{2}$$

Furthermore, all parts of Equation 2 are divided into dry and moist energy transport (Equation 3), where the moist part consists the transport of energy via latent heat and the dry part consists the transport of potential energy and sensible heat.

$$
\begin{aligned}
AHT &= AHT_{moist} + AHT_{dry} \\
MOC &= MOC_{moist} + MOC_{dry} \\
SE &= SE_{moist} + SE_{dry} \\
TE &= TE_{moist} + TE_{dry}
\end{aligned}
\tag{3}
$$

The total MHT at a latitude circle can be calculated with dynamic and energetic approaches, where in the energetic approach the MHT is balanced by the spatial integral of the net radiative deficit at the TOA and in the dynamic approach MHT is the vertically and zonally integrated net transport of energy. Here we use the energetic approach to calculate MHT (Equation 4)

$$MHT(\Phi) = 2\pi a^2 \int_{-\frac{\pi}{2}}^{\Phi} \cos\Phi' \left[ASR(\Phi') - OLR(\Phi') \right] d\Phi', \tag{4}$$

where ϕ is the latitude circle, a is the radius of the Earth, ASR is the absorbed solar radiation, OLR is the outgoing longwave radiation. The boundary condition is that the transport has to be zero at the pole, because non-zero values have no physical meaning. To fulfill the boundary conditions at both poles, we need to balance the global budget. For this we assume that the imbalance is spatially uniform, thus the area-weighted global average energy imbalance is subtracted at all latitudes before calculating the integral in Equation 4. In our ensemble the mean of the global imbalance is approximately 0.4 W/m², where among all simulations the largest imbalance is 1.95 W/m² (COSMOS $1 \times CO_2$) and the smallest is 0.01 W/m² (CESM piControl).

OHT can also be calculated with the energy approach from the surface heat fluxes (SHF) (Equation 5)

$$OHT(\Phi) = 2\pi a^2 \int_{-\frac{\pi}{2}}^{\Phi} \cos\Phi' \left[SHF(\Phi') \right] d\Phi', \tag{5}$$

where SHF is positive downward. The above equation is true with the assumption that the ocean is in equilibrium, so the heat storage is negligible. If the ocean is not in an equilibrium state, then Equation 5 represents the implied OHT, which is the sum of OHT and the spatial integral of the tendency of ocean heat content. The DeepMIP simulations have been required to fulfill different criteria to prove that they reached the equilibrium state. The criteria considered the length of the simulations, the radiation imbalance at the TOA, and the ocean's equilibrium state. All of the included simulations satisfy at least two of the three criteria, with the only exception of CESM at $3 \times CO_2$, which is still close to both missed criteria, thus all, here considered simulations, have been accepted to be sufficiently equilibrated (Lunt et al., 2021). We consider Equation 5 defining OHT and that balancing the global radiative budget at the TOA does not largely affect the calculation of MHT.

After calculating MHT and OHT given Equation 1 AHT is known as the residual. The direct dynamical calculation of AHT is formulated via the vertically and zonally integrated meridional transport of moist static energy (MSE):

$$MSE = c_p T + Lq + gZ$$

$$AHT(\Phi) = \frac{2\pi a \cos \Phi}{g} \int_0^{P_s} \left[\overline{V}\right]\left[\overline{MSE}\right] + \left[V^* MSE^*\right] + \left[\overline{V'^* MSE'^*}\right] + \overline{\left[V\right]'\left[MSE\right]'} dp, \quad (6)$$

where cp is the specific heat capacity of air at constant pressure, T is temperature, L is the latent heat of vapourization of water, q is the specific humidity, g is the acceleration of gravity, Z is the geopotential height, P_s the surface pressure, V is the meridional velocity. The square brackets $[x]$ denote zonal averages, the overbars $\overline{x}$ denote time averages (monthly means), x^* denote zonal anomalies, and x' means time anomalies. In Equation 6 the first term defines the energy transported via MOC the second is SE, the third is TE, and the last one has been referred as the transient overturning circulation (TOC) (Marshall et al., 2014), which is two orders of magnitudes smaller than MOC at the tropics and the eddy terms at midlatitudes. Thus, we do not try to consider TOC on its own, but handle it together with TE. Note that the calculation of TE and TOC would require high temporal resolution data, which is not available for the DeepMIP simulations, thus we cannot calculate AHT only from Equation 6, hence we use the residual method via Equation 1. Nevertheless, the transport via MOC and SE is calculated from Equation 6 with monthly mean data. The remaining atmospheric transport, which we refer to as TE, is again defined with a residual method. This TE calculation, has been shown to be successful in calculating the partitions from monthly mean data with good accuracy (Donohoe et al., 2020).

Regarding the moist and dry partitioning for AHT we define AHT$_{moist}$ as the latent heat transport at a given latitude, which is the integral of evaporation (E) minus precipitation (P) multiplied by the latent heat of vapourization:

$$AHT_{moist}(\Phi) = 2\pi a^2 \int_{-\frac{\pi}{2}}^{\Phi} \cos \Phi' \left\{ L\left[E(\Phi') - P(\Phi')\right]\right\} d\Phi'. \quad (7)$$

The dry contribution to AHT is then calculated by subtracting the moist part from the total (Equation 3). The moist and the dry parts of MOC and SE are calculated via Equation 6, but MSE has been split into dry, the sensible heat and potential energy ($c_p T + gZ$) and moist part, the latent heat (qL) (Donohoe et al., 2020). The moist and dry contributors to TE can be calculated via the residual method, with the use of Equation 3 and:

$$AHT_{moist} = MOC_{moist} + SE_{moist} + TE_{moist}.$$

2.5. Meridional Streamfunction

There are several metrics to quantitively analyze the Hadley cell, its edge and its circulation strength. We choose to use the average meridional streamfunction Ψ (Xian et al., 2021) to quantify its intensity, which is defined as:

$$\Psi(p, \Phi) = \frac{2\pi a \cos \Phi}{g} \int_0^{P_S} [V] dp.$$

A stronger streamfunction means a stronger Hadley cell circulation. For the vertical integral, the zonal mean meridional wind values are taken from pressure levels, to where they were interpolated from each models' sigma or hybrid sigma-pressure vertical coordinate system.

2.6. Monsoon Area

The monsoon climate is characterized by seasonal reversal of prevailing surface winds which results in a rainy summer and dry winter. To assess the geological area where monsoon was probably present in the EECO, we use a simple monsoon definition, which is also used in the sixth Assessment Report of IPCC (IPCC, 2021). The global monsoon is defined as the area, where the local annual range of precipitation exceeds 2.5 mm per day (Kitoh et al., 2013). The annual range is defined by the local summer- minus-winter precipitation, that is, MJJAS

minus NDJFM in the Northern Hemisphere and NDJFM minus MJJAS in the Southern Hemisphere. The 2.5 mm per day threshold is defined based on current conditions, which might not hold so well in a warmer world, nevertheless we accept it for our rough estimations. We tested other identification methods for example, one where the change in precipitation is considered in percentages (Wang & Ding, 2008), and it led to similar conclusions regarding the global monsoon area change. A more detailed analysis of the monsoon systems is to follow this study, where not just the resulting precipitation, but the dynamical aspects of the monsoon systems are to be studied. Considering also the wind circulation regarding the monsoon systems, will help to eliminate possible precipitation related biases from the models.

3. Results

3.1. Preindustrial Control Simulation

We start our analysis by evaluating the selected models' representation of present day climate, more precisely the climate of the preindustrial period. To assess the models' results we compare them to transport values calculated from the ERA5 reanalysis from 1991 to 2020. Note that this comparison is not entirely fair since the models and the reanalysis represent two different climate periods approximately 150 years apart, and in this one and a half century the climate constraints, especially the CO_2 concentration have changed. Nevertheless, the CO_2 change is still notably smaller than in the Eocene simulations and both models and reanalysis represent a climate with current topography, continental ice sheets and relatively similar meridional temperature gradient, when compared to our knowledge of EECO's climate. Thus, we accept these discrepancies and focus on the structure of the transport processes, and not on the quantitative amounts.

The MHT and its partitions calculated from the DeepMIP models and the ERA5 reanalysis are shown in Figure 1. Overall, there is good agreement between the mean of the model ensemble and the reanalysis. The values and distributions of the MHT and its components fit well also to previous studies which are based on observations and reanalysis (Donohoe et al., 2020; Masuda, 1988). We calculated the average of the transport processes for 6 zonal bands (South Polar S90°–S60°, South Midlatitude S60°–S30°, South Tropics S30°–0°, North Tropics 0°–N30°, North Midlatitude N30°–N60°, North Polar N60°–N90°) and found that the average difference between the ensemble mean and the reanalysis among these zonal bands is 0.07 PW. Also, the best agreement is at the North Polar band and the worst is at the North Tropics.

MHT reaches maximum of above 5 PW at around 40° both South and North. The ocean transports more heat than the atmosphere in a narrow tropical belt (0°N–10°N), outside of which the atmospheric heat transport dominates (Figure 1a). The reanalysis is within the spread of the DeepMIP ensemble. The ensemble mean fits the reanalysis better over the Southern Hemisphere than over the Northern Hemisphere, where the models transport more via the atmosphere and less via the ocean. These two compensate each other resulting in a good fit for the total MHT.

The atmospheric transport partitioned into latent heat and dry static energy transport (Figure 1c) shows that the two have similar order of magnitude, but the dry static energy transport is at all latitudes poleward, while the latent heat transport is equatorward in the tropics and poleward at the rest of the latitudes.

Partitioning of the atmospheric heat transport into MOC, stationary, and TE shows that transport is (a) mainly in TE in the midlatitudes, that is, in extratropical cyclones, and (b) dominantly by MOC, that is, by the Hadley cells, in the tropics (Figure 1b). The separation of the MOC into its dry and moist parts (Figure 1e) reflects the poleward transport of potential and sensible heat in the upper part of the Hadley cell and the equatorward latent heat transport in the lower part of the Hadley cell. The transport of the two parts do not balance out each other resulting in a net poleward energy transport. SE show importance in the poleward latent heat transport around 30° in both hemispheres, representing the monsoon systems (Figure 1d). Extratropical cyclones transport heat in both, the moist and dry form (Figures 1b and 1f).

3.2. Effect of the Non-CO_2 Forcing on the Eocene MHT

The Eocene $1 \times CO_2$ simulations, that is, with non-CO_2 forcing because of changes in paleogeography and vegetation or the lack of continental ice sheets, are 3–5°C warmer than the preindustrial simulations (Lunt et al., 2021). Figure 2 shows the MHT differences between the Eocene $1 \times CO_2$ and the PI simulation. There is more southward MHT in the $1 \times CO_2$ simulation than in the preindustrial one, which is mainly due to an increase
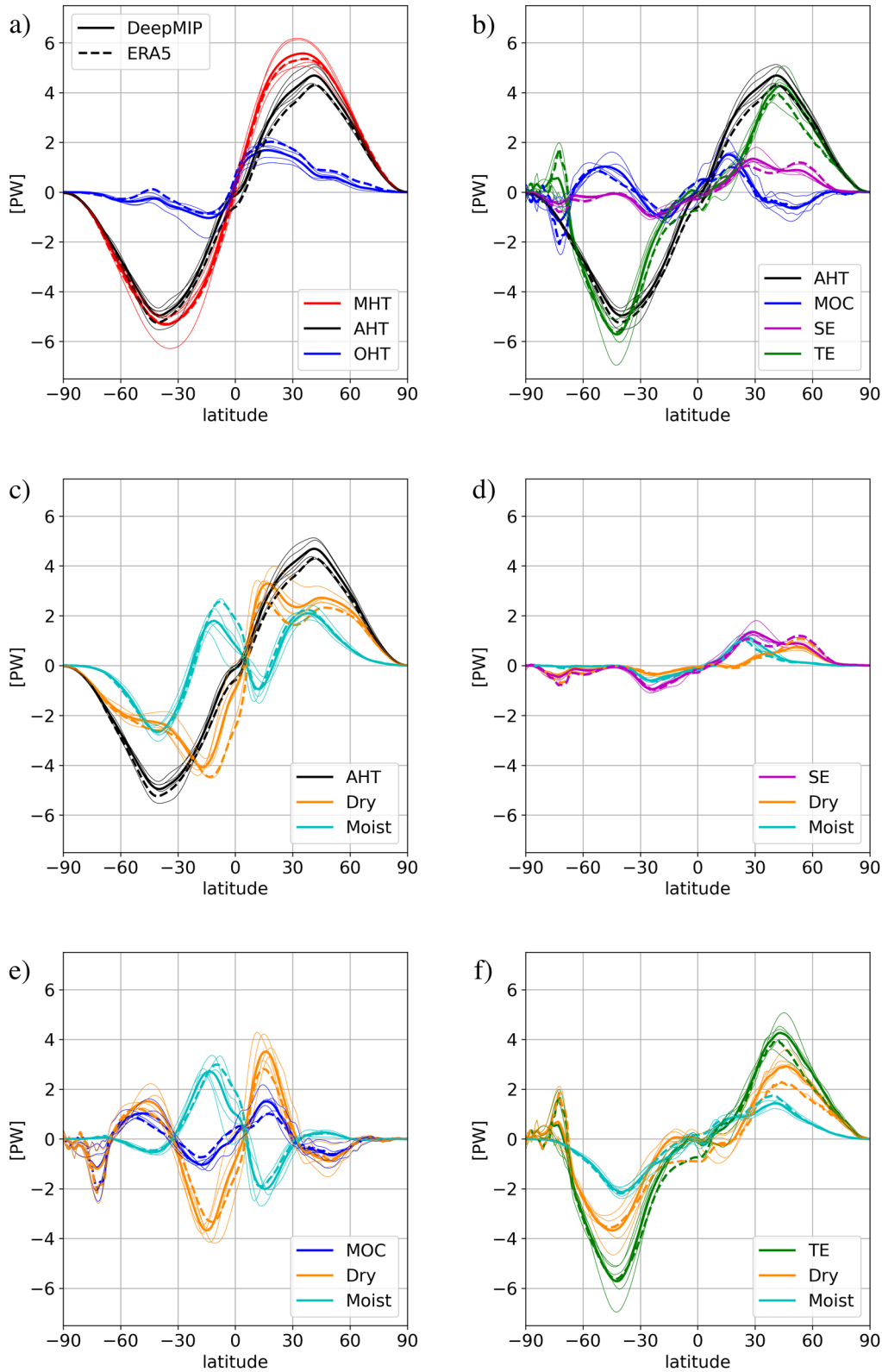
Figure 1.

in the oceanic southward heat transport (Figure 2a). This results in smaller poleward MHT in the Northern Hemisphere but larger in the Southern Hemisphere during the Eocene, so the heat transport shifts toward the south. In other words, due to the Eocene boundary conditions the ocean transports more heat toward the South Pole, approximately 50% more than in the preindustrial simulation, over the Southern Hemisphere and approximately 25% more toward the south from the Northern Hemisphere, while the atmosphere partially compensates these changes via more heat transport toward the North Pole.

The change in atmospheric dry and moist transport is also asymmetric. Over the Northern Hemisphere there is more moisture transport equatorward in the tropics and more poleward transport at midlatitudes, while the dry static energy transport compensates these changes, with more poleward transport at the tropics and less at higher latitudes (Figure 2c). On the other hand, over the Southern Hemisphere the tropical equatorward latent heat transport decreases and the extratropical poleward latent heat transport increases. The poleward dry static energy transport decreases at all southern latitudes. These together lead to a net increase in atmospheric poleward transport in the Northern Hemisphere and a decrease in the Southern Hemisphere, which as mentioned above is overcompensated by the ocean. An increase in poleward latent heat transport also has an important role in polar amplification.

The most prominent atmospheric change is the increased heat transport by TE between 30°N and 60°N (25% increase) and 60°S–90°S (110% increase) (Figure 2b). These represent heat transport by extratropical cyclones, thus cyclones are more frequent and/or more intense in the Eocene simulations. To quantify the number of cyclones and their features, more frequent than monthly model output would be needed. The increased TE transport is mostly compensated by SE and MOC transports (Figure 2b). There is also a decrease in the Northern Hemisphere monsoonal transport (Figure 2d). The Hadley circulation also shows an asymmetric shift, with more energy being overturned in the northern cell, and less in the southern one, while the net poleward MOC energy transport of the tropical band stays close to the control simulation (Figure 2e).

3.3. Effect of the CO_2 Forcing on the Eocene MHT

The effect of higher CO_2 concentrations on early Eocene transport processes is studied by quantifying the changes between the $3 \times CO_2$ and $1 \times CO_2$ simulations, and also where possible the changes between $6 \times CO_2$ and $3 \times CO_2$ simulations (Figures 3 and 4). We show the changes due to the two stepwise CO_2 increase on one figure (Figure 4) to display the relation of the transport change signal to the CO_2 rise. Our chosen DeepMIP ensemble has five models available with $3 \times CO_2$ simulations and only two with $6 \times CO_2$ simulations (CESM and GFDL, see Table 1). The two latter simulations are shown to be the most successful in representing the global mean surface temperature, global mean SST and global meridional SST gradient when compared to proxy data (Lunt et al., 2021).

When comparing the changes relative to the equator, we see mostly symmetric changes, thus the effect of CO_2 rise is global and influences both hemispheres in a similar way. For the $3 \times CO_2$ simulation we find an increase in poleward MHT compared to the $1 \times CO_2$ simulation, which mainly results from the atmosphere (Figure 3a). The MHT change between $6 \times CO_2$ and $3 \times CO2$ fluctuates around zero (Figure 4a). In this case the OHT catches up with the change in the AHT and counteracts it more, that is, the BJC is more prevalent. Nevertheless, both from $1 \times CO_2$ to $3 \times CO_2$ and from $3 \times CO_2$ to $6 \times CO_2$ concentration, the ensemble mean poleward AHT increases and OHT decreases. Polar amplification is also represented via the increased latent heat transport from the subtropics toward the poles, compensated by the dry static heat transport (Figures 3c and 4c). Regarding the different physical processes in the atmosphere, we see similar changes from $1 \times CO_2$ to $3 \times CO_2$ and from $3 \times CO_2$ to $6 \times CO_2$ (Figure 4b). The changes in transport processes are the same or larger during the first increase as during the second step. For example, in the northern Hadley cell from $1 \times CO_2$ to $3 \times CO_2$, the sensible and latent heat transport increase with 35% and 47% respectively, while from $3 \times CO_2$ to $6 \times CO_2$ they increase only a further 16% and 23%. This shows a slight nonlinear behavior of the transport processes in relation to CO_2 change. At the tropics
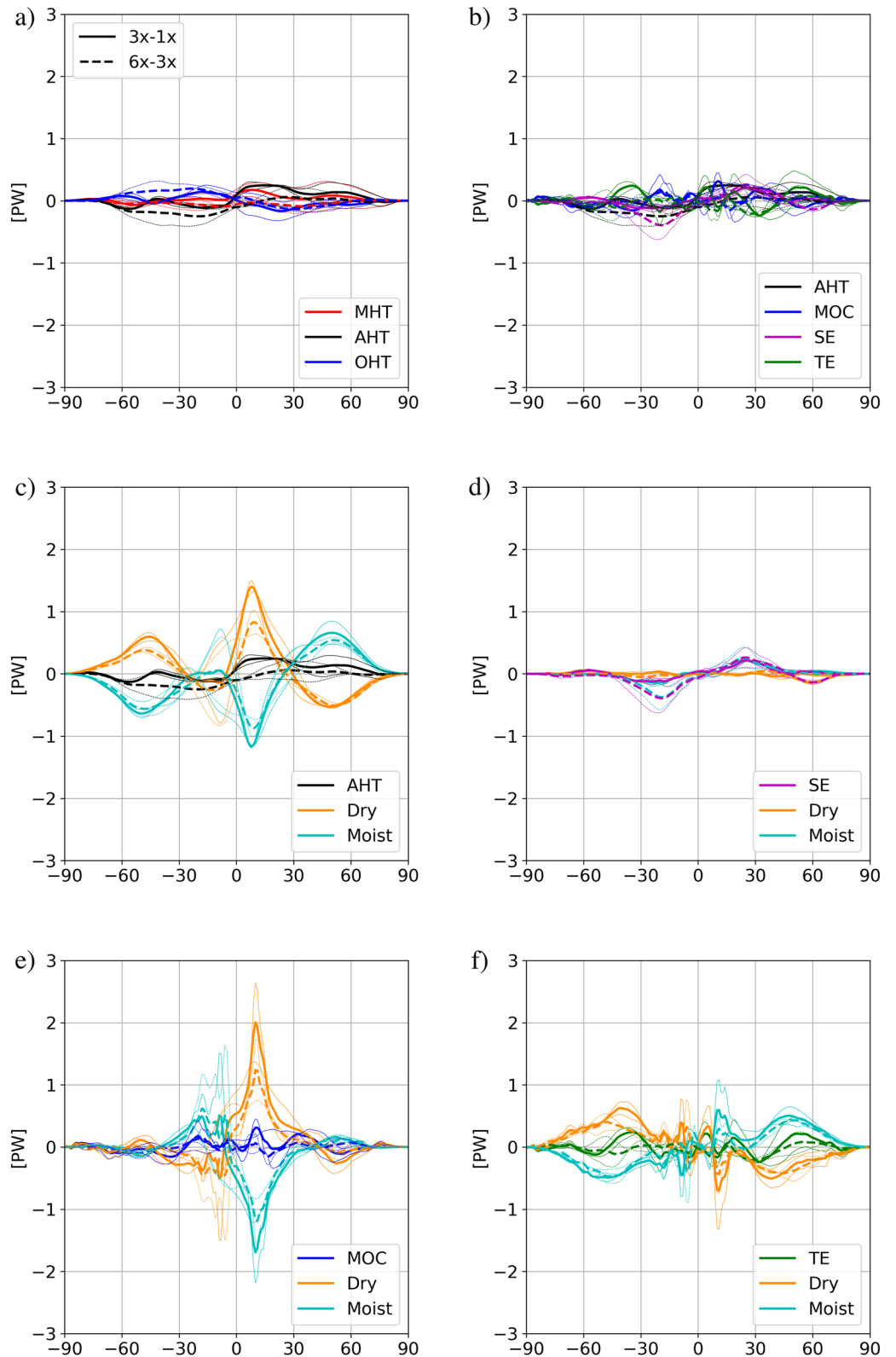
Figure 1. Annual meridional heat transport (MHT) and its different parts in the preindustrial control simulations of the five Deep-Time Model Intercomparison Project ensemble members and the ERA5 reanalysis. Bold lines representing the ensemble mean thin lines representing each model and dashed lines are calculated from ERA5 (1991–2020) reanalysis. The partitions of MHT are (a) MHT, divided between atmospheric (AHT) and oceanic (OHT) part, (b) atmospheric transport divided into meridional overturning circulation (MOC), Stationary Eddies (SE) and Transient Eddies (TE), (c) atmospheric transport divided to dry and moist parts, (d) atmospheric transport via SE and its dry and moist parts, (e) atmospheric transport via MOC and its dry and moist parts, and (f) atmospheric transport via TE and its dry and moist parts.
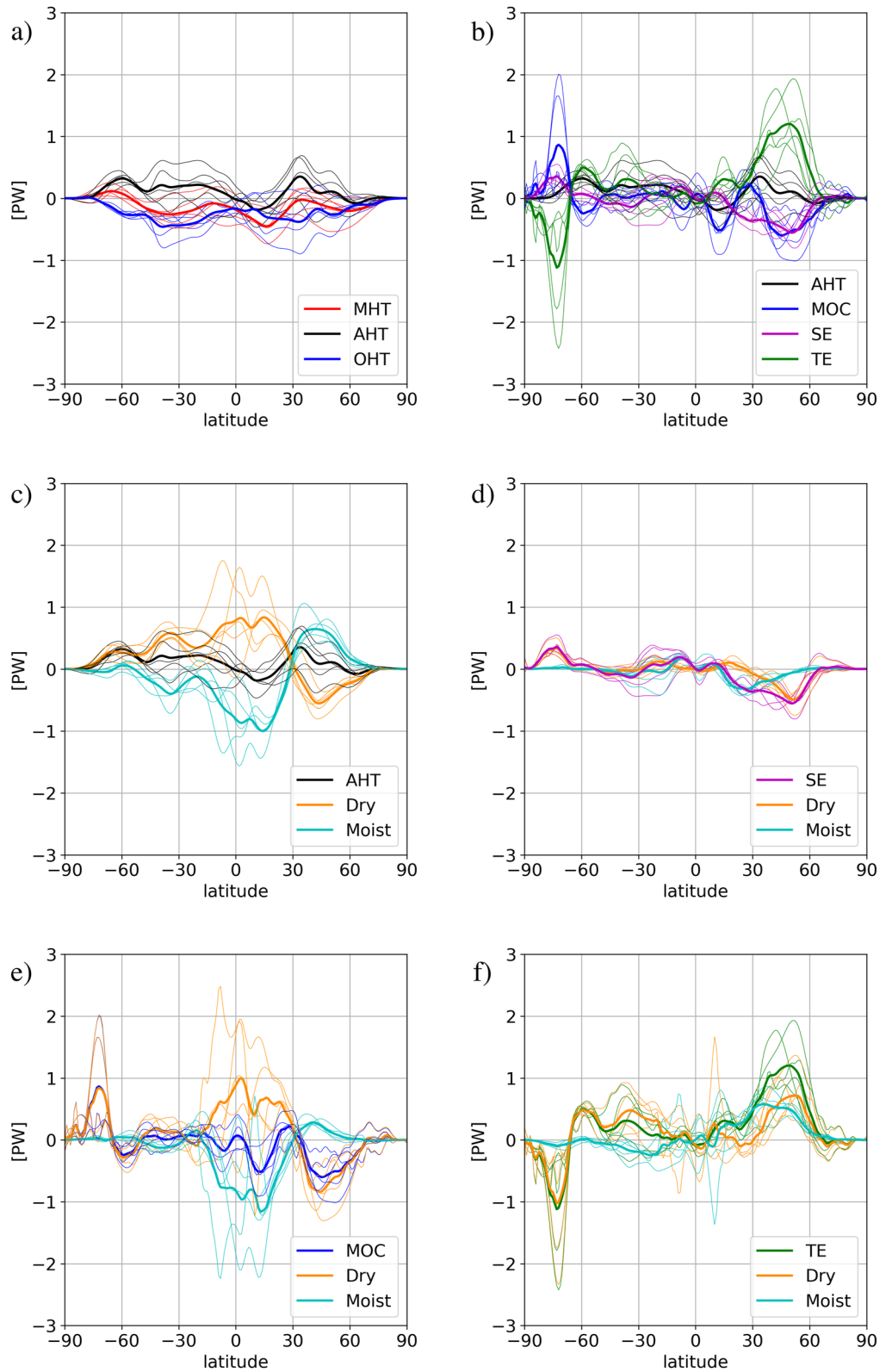
Figure 2. Meridional Heat Transport and its parts, same as Figure 1, but showing the differences between the $1 \times CO_2$ Eocene and the preindustrial control simulations.
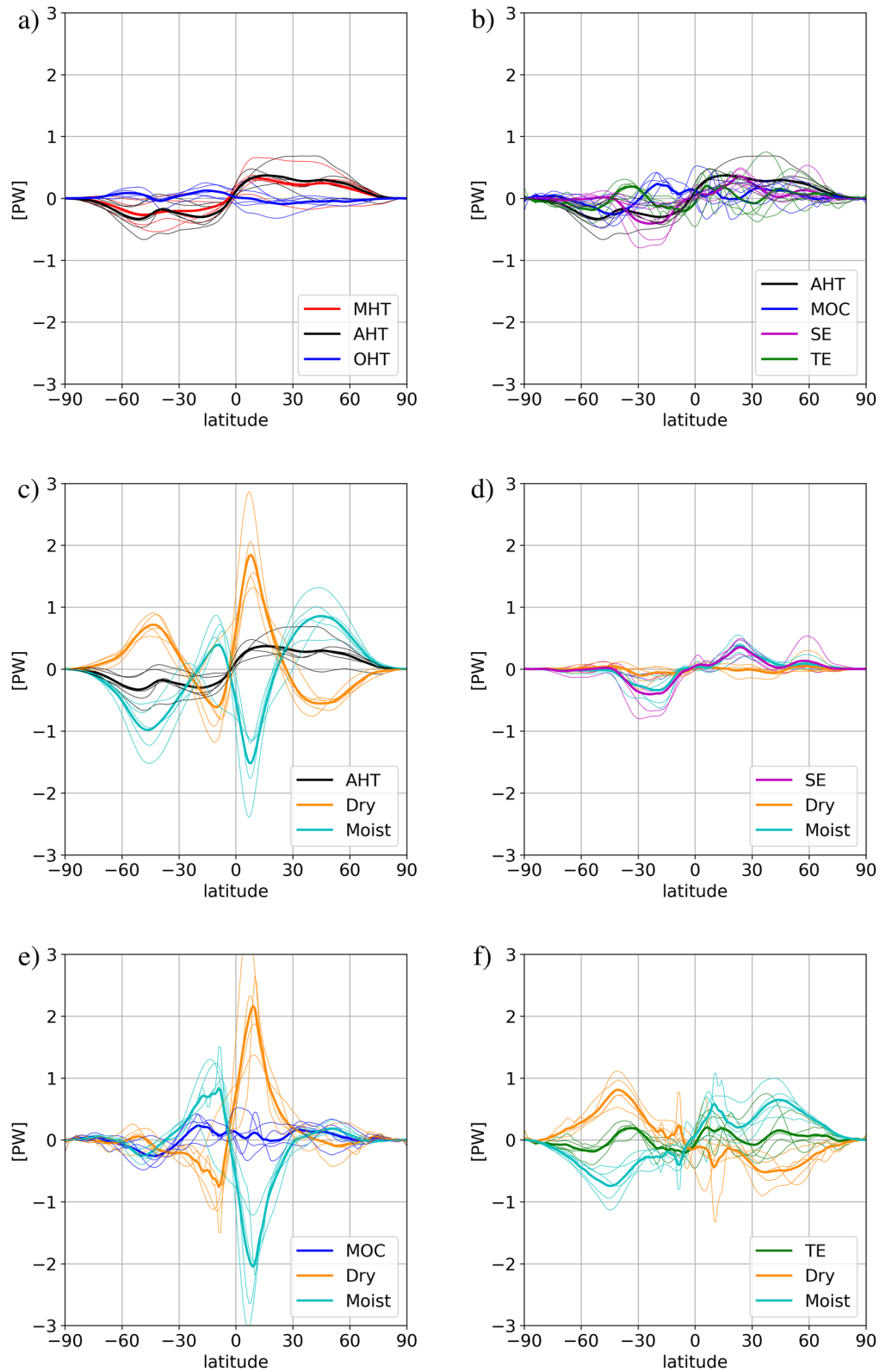
Figure 3. Meridional Heat Transport and its parts, same as Figure 2, but showing the differences between the $3 \times CO_2$ and the $1 \times CO_2$ paleo simulation.

Figure 4. Meridional Heat Transport and its parts, same as Figure 3, but showing the differences between the $6 \times CO_2$ and the $3 \times CO_2$, and the $3 \times CO_2$ and the $1 \times CO_2$ paleo simulations. The ensemble here consists of only two models: Community Earth System Model, Geophysical Fluid Dynamics Laboratory.

the energy transport due to the MOC is slightly decreases, but the poleward dry static and the equatorward latent heat energy transport of the Hadley cells increase more so at the northern cell than at the southern one (Figures 3e and 4e). The subtropics, are mostly defined by the increased poleward transport of moist SE (Figures 3 and 4d), thus the monsoon systems transport more energy in the higher CO_2 simulations. At midlatitudes the poleward transport of TE increases slightly (Figures 3f and 4f), but the magnitude of change is smaller than, what the non-CO_2 constraints caused in the $1 \times CO_2$ simulations (see Figure 2f).

3.4. Effect of the Total Forcing on the Eocene MHT

Finally, we investigate the overall heat transport changes between the simulated preindustrial and the most-likely Eocene climate states. This is important as it is the relevant change when comparing Eocene proxy data to present day conditions, and because the individual changes due to the CO_2 and the non-CO_2 constrains are potentially nonlinear and can counteract each other.

In total MHT, we see more changes compared to the present day climate in the Northern Hemisphere, where the atmosphere transports more energy while the ocean compensates this with less transport (Figure 5a). There is an increase of latent heat transport toward the polar regions at both hemispheres in the EECO climate, which is compensated by the decrease in dry static energy transport at the midlatitudes (Figure 5c). In the tropics the net poleward transport via MOC is slightly less than the preindustrial values, but the dry (poleward) and moist (equatorward) energy transport increases inside the Hadley cell, especially in the northern cell (Figure 5e). In the southern subtropics the EECO simulations show slightly more latent heat transport via SE (Figure 5d). This means that the monsoon systems in the Southern Hemisphere transported more energy during the EECO. Nevertheless, it has been shown in the previous two subsections that the monsoon in the Northern Hemisphere also changed, but with opposite signs due to the respective CO_2 and non-CO_2 forcings. Thus, the overall monsoonal transport changes in the Northern Hemisphere are small. At the midlatitudes, especially in the Northern Hemisphere more energy is transported via TE (cyclones) during the Eocene, which is again compensated by less transport via SE (Figure 5b, 5d, and 5e). In the Southern Hemisphere we find slightly less transient eddy transport in the EECO than in the preindustrial simulations.

4. Discussion

Our results showed that the change in transport processes due to non-CO_2 forcings are asymmetric to the Equator, while the global CO_2 concentration increase caused rather symmetric changes in the transport processes. Regarding the total MHT we found that the paleo set up caused a shift in the heat transport toward the South Pole, mainly through an increase in OHT. This, we hypothesize, is connected to the location of deepwater formation in the Eocene ocean, which presented itself in the Southern Ocean in the DeepMIP models, with the exception of the GFDL model, where it occurred in the North Pacific (Zhang et al., 2022). Thus, the deepwater formation, which occurs in the North Atlantic in the present, most probably was shifted toward the Southern Hemisphere in the Eocene, which most probably resulted in an increase in the OHT toward the South Pole. This is in line with the results of Brady et al. (1998), who showed that in the Late Cretaceous the poleward OHT was also larger at that hemisphere, where the deepwater formation occurred. The mostly symmetric changes due to CO_2 forcing is explained by the fact that it is a global forcing, and with the Eocene's ice free set up. It has been shown that a lower topography of Antarctica decreases the asymmetry between the Arctic and Antarctica (Salzmann, 2017). The lack of continental ice sheet in Eocene simulations also balances other feedback mechanisms such as the surface albedo, laps rate and water vapor feedback, between the two polar regions (Lunt et al., 2012).

The analysis of the different transport processes identified those large scale circulation patterns, which are either effected by the changes in the paleo set up or by the changes in the CO_2 concentration. These, heading from the tropics to the pole, are the Hadley cell, the monsoon and the mid-latitude cyclones. In the next subsections we discuss the changes in these large scale patterns in more detail.

4.1. Hadley Cell

We found that both the CO_2 and non-CO_2 constraints have an asymmetric effect on the Hadley cells. In case of the non-CO_2 constraints, we see a northward shift, namely that the northern cell circulates more heat while the southern cell circulates less than in the control simulation (Figure 2e). Nevertheless, when considering the net poleward
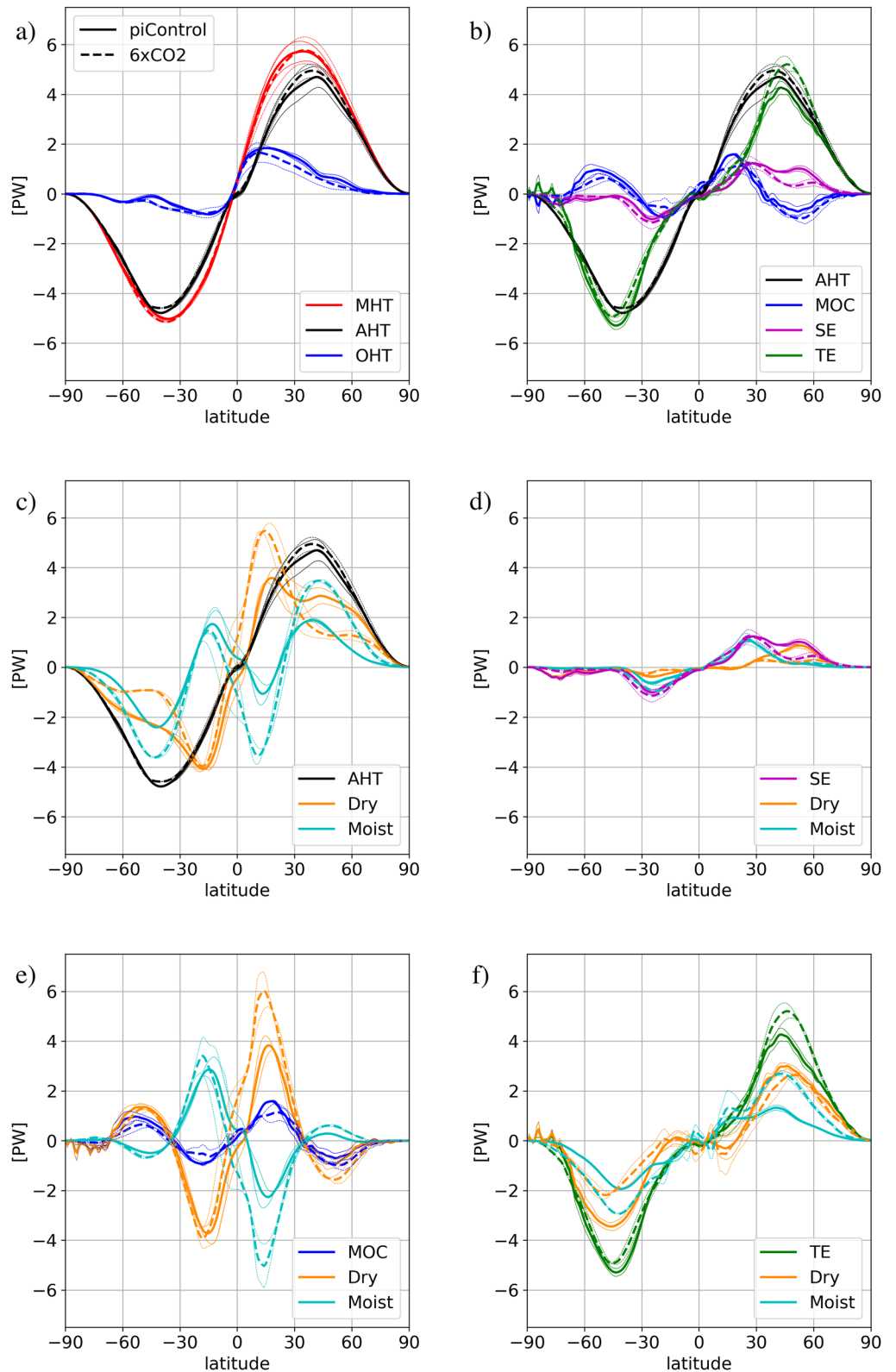
Figure 5. Meridional Heat Transport and its parts, same as Figure 1, but showing the preindustrial control (solid lines) and $6 \times CO_2$ (dashed lines) simulation results. The included models are: Community Earth System Model, Geophysical Fluid Dynamics Laboratory.

Table 2
Streamfunction Maximum and Minimum Values [1E + 10 kg/S] in the Different Models and Simulations and in the ERA5 Reanalysis, Indicating the Intensity of Each Hadley Cell

| 1E + 10	CESM		GFDL		HadCM3		COSMOS		MIROC		ERA5	
	South	North	South	North	South	North	South	North	South	North	South	North
piControl	−10.1	8.8	−7.8	8.2	−9.2	9.6	−9.1	7.3	−10.6	7.3	−11.0	7.8
$1 \times CO_2$	−6.1	7.4	−6.7	7.6	−9.0	13.5	−8.7	9.2	−9.2	8.8		
$3 \times CO_2$	−5.5	6.7	−5.1	6.8	−7.9	13.3	−8.1	8.6	−8.4	9.9		
$6 \times CO_2$	−5.4	6.6	−4.2	6.5								

MOC heat transport, the southern cell transports nearly the same as in the control simulation and the northern cell transports slightly less energy poleward. In the case of CO_2 increase, the net poleward MOC transport of Hadley cells, change relatively evenly (0%–20% decrease for the tropical band), but inside each cell more heat is circulated, and the changes are notably larger in the northern cell (Figures 3e and 4e). Since all these simulations have a generally warmer climate than the control simulation it means, that part of the surplus energy compared to the preindustrial simulation, is coming from the higher temperatures and higher water holding capacity of the atmosphere. When using the streamfunction for investigation the Hadley circulation in the high CO_2 simulations, all models show a weakening intensity of the southern cell. The intensity of the northern cell is strengthening in HadCM3, MIROC, and COSMOS, while CESM and GFDL show a slight weakening (see Table 2). Figure 6 shows the cross sections for the model simulations. The southern cell's intensity is decreasing with the CO_2 rise, while the northern cell's intensity slightly increases. A change in the edge of the cells is not assessed here, because the models' resolution is too low for it to be precisely estimated. Nevertheless, the cross sections visual evaluation shows a southward expansion of the northern cell (Figure 6), which might be partially explained by the paleo-geography. In the Eocene, less continental land areas were located in the northern tropical belt. This could lead to a relative southward shift of the Intertropical Convergence Zone (ITCZ), given that during the summer half year the ITCZ travels poleward mostly over the continental areas. Nevertheless, the reason for the hemispheric asymmetry in overturned energy, intensity and position between the northern and southern Hadley cells is not entirely clear. Hemispheric asymmetry in the Hadley cells due to CO_2 forcing has been projected by climate models under present day conditions as well, but with an opposite sign, namely projecting larger expansion in the southern Hadley cell (Watt-Meyer et al., 2019). One possible reason for this different asymmetry, namely that in the Eocene under high CO_2 conditions, we see larger changes in energy transport in the northern Hadley cell, while future high CO_2 projections predict larger extension of the southern Hadley cell, might be connected to the change in ocean circulation, and the hemispheric switch in deepwater formation. Moreover, in present day climate, an upwelling cools the surface of the Southern Ocean, and by this, increases the meridional temperature gradient (Watt-Meyer et al., 2019). Under Early Eocene conditions this upwelling was most likely not present (Sarkar et al., 2019), which can further contribute to the change in hemispheric asymmetry.

4.2. Monsoon

In the subtropics the transport via moist SE represents the heat transport by monsoon systems. The analysis of the non-CO_2 effects showed a decrease in their transport in the Northern Hemisphere and the CO_2 effects analysis showed an increase in transport with the CO_2 rise. Thus, we investigated the monsoon area to better evaluate these changes. The monsoon area is defined by the annual precipitation range (Kitoh et al., 2013) in all simulations.

In Figure 7 the monsoon areas are plotted from the CESM preindustrial 1×, 3× and $6 \times CO_2$ concentration simulation. Paleogeography plays an important role in defining monsoon areas as is shown by the smaller monsoon area in the early Eocene set-up than in the preindustrial. From the preindustrial to the $1 \times CO_2$ simulations, the percentage of monsoon areas decreases in all models, except COSMOS (see Table 3). The mean of the ensemble shows that in the preindustrial simulations the monsoon covers 18.7% of the globe, while in the $1 \times CO_2$ this area is reduced to 15.3%. This correlates well with the slight decrease in the transport of moist SE in the subtropics (Figure 2d). From the 1× to the 3× and to the $6 \times CO_2$ simulations (for CESM), the monsoon area increases with higher CO_2 values (Figure 7). This also correlates well with the results seen in the transport figures, where there is an increase in moist stationary eddy transport in the subtropics (Figures 3 and 4d). The only exception from the increase of monsoon area with CO_2 rise, is GFDL with a decrease in monsoon area from the 3× to the 6×CO_2 simulation.
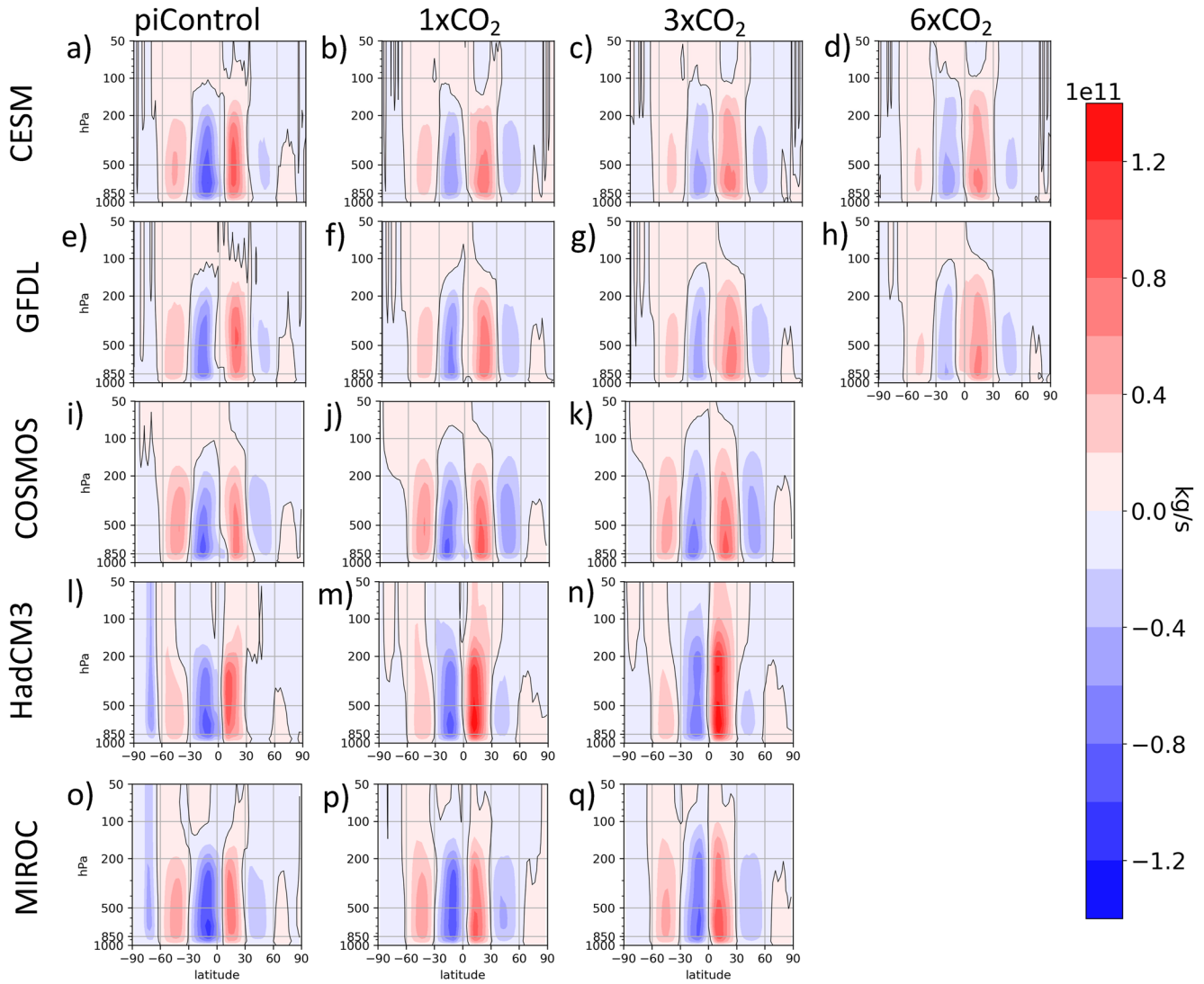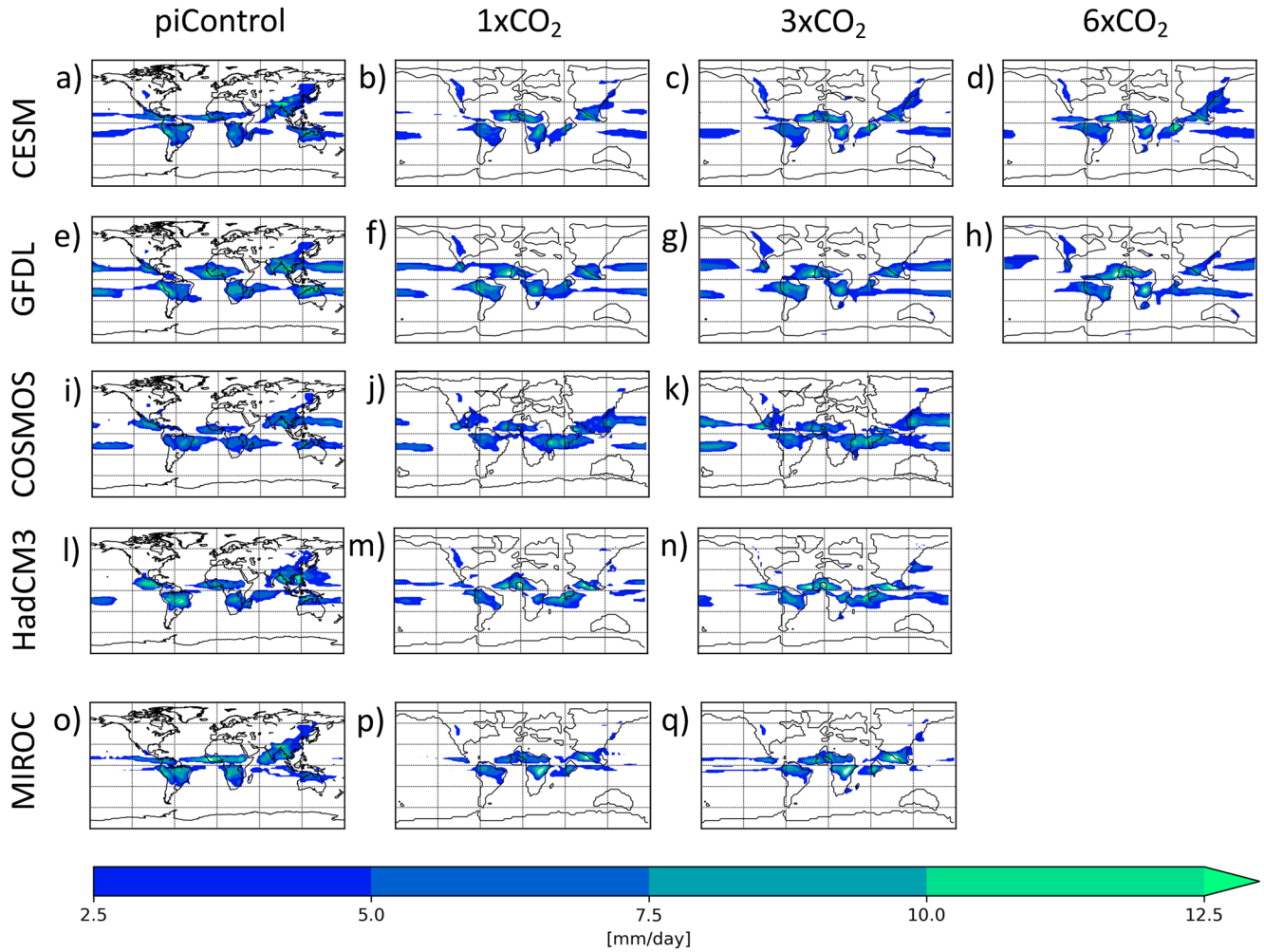
Figure 6. Cross section of the annual mean meridional streamfunction in the preindustrial control, $1 \times CO_2$, $3 \times CO_2$, and when available, $6 \times CO_2$ simulations in the five different models.

When comparing the preindustrial climate to the EECO, namely the preindustrial simulations to the $6 \times CO_2$ simulations for CESM and GDFL simulations, we see that the effect of the non-CO_2 constraints (smaller monsoon area in the Eocene) and the effect of the CO_2 forcing (higher water holding capacity of the warmer atmosphere) compensate each other in terms of the energy being transported. This agrees well with the findings of Licht et al. (2014), who investigated proxy data from Asia in the late Eocene (gastropod shells and mammal teeth from Myanmar, and aeolian dust deposition in northwest China) and found monsoon like patterns in rainfall and wind. They also concluded that the enhanced greenhouse gas concentrations compensated the negative effect of lower Tibetan relief on precipitation, which reduces the East Asian monsoon strength (Tang et al., 2013). In summary, when comparing present and EECO monsoon systems from the energetic point of view, there is no large difference (Figure 5d), nevertheless the reason for this is due to compensating mechanisms. Note that this does not indicate that there is no significant change in monsoon precipitation intensity.

4.3. Midlatitude Cyclones

We found that in the paleo set up even without the CO_2 increase, more energy is being transported via midlatitude cyclones especially in the Northern Hemisphere (Figure 2b). This can be explained by an increase in semi-permanent low pressure systems, in other name centers of action, in the Eocene simulations. In Figure 8 the

Figure 7. Monsoon area defined by the annual precipitation range (summer minus winter) with the unit of mm/day, in the preindustrial control, $1 \times CO_2$, $3 \times CO_2$, and when available, $6 \times CO_2$ simulations in the five different models.

sea level pressure anomalies are representing these centers of action. In the Northern Hemisphere in the preindustrial simulation one can identify two main low pressure systems during winter (Figure 8a), the Icelandic and the Aleutian lows, while in the Eocene even four low pressure centers can be identified. We call these the Icelandic, the Aleutian, the Gulf of Alaska and the Eurasian Low (Figure 8c).

The development of these semi-permanent pressure features is connected to the thermal contrast between the ocean and the continent during winter, due to the different heat capacity of land and sea. This also explains why the semi-permanent pressure systems develop differently in the paleo set up. In the Eocene world there was a wider Pacific basin and a narrower Atlantic basin together with the existence of the Turgai Sea or West Siberian Sea, an epicontinental sea separating Europe from Asia. The existence of the West Siberian Sea, which is located

Table 3
Global Monsoon Area in Percentages in the Different Models and Simulations

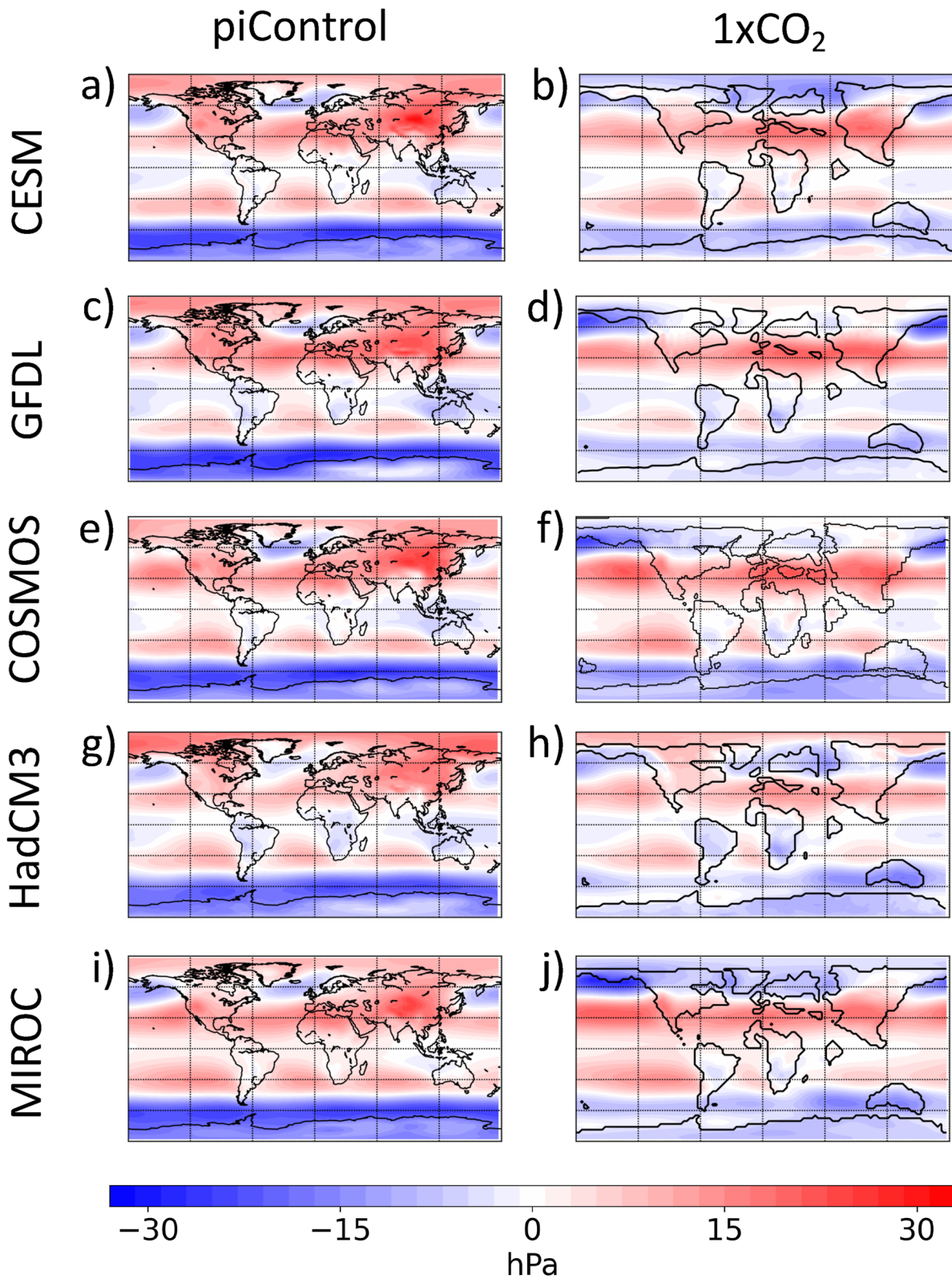|	CESM	GFDL	HadCM3	MIROC	COSMOS	ENS	ERA5
piControl	18.83	21.87	17.97	16.36	18.45	18.70	17.46
$1 \times CO_2$	14.61	19.17	13.59	10.47	18.64	15.30	–
$3 \times CO_2$	14.91	19.95	14.26	12.75	22.43	16.86	–
$6 \times CO_2$	15.42	18.04	–	–	–	16.73	–

Figure 8. Winter sea-level pressure anomaly in the different models in the preindustrial control simulation (left) and in the $1 \times CO_2$ paleo simulation (right).

in the northern midlatitudes, lead, in the models, to the development of an Eurasian Low pressure system that is not in present in the modern times. The wider Pacific basin and the presence of the Bering land bridge lead, in the models, to a split in the Aleutian Low, so in the Eocene both an Aleutian Low and a Gulf of Alaska Low are present in the simulations. In the Southern Hemisphere the position of the Antarctic continent did not change much and, thus, the pressure systems in the models developed similarly as in the present climate (Figures 8b and 8d).

The TE' energy transport increase in the $1 \times CO_2$ paleo simulations, are partly the result of these simulations' warmer atmosphere. Nevertheless, we also hypothesize that the energy transport increase is also related to an increase in cyclonic activity due to more semi-permanent low pressure systems over the northern midlatitudes. This can mean more and/or deeper cyclones than in the present climate. To quantitatively assess this, the model output in our study with the monthly temporal resolution is insufficient.

5. Conclusions

In this study we calculated and analyzed the MHT and its partition in the atmosphere in climate model simulations of the preindustrial and the EECO. We used simulations from five climate models (CESM, COSMOS, GFDL, HadCM3, and MIROC) provided by the DeepMIP community. The transport values are calculated from monthly mean data, and we distinguish between the different physical mechanisms, which transport energy in the atmosphere. The impacts of the non-CO_2 related conditions (paleogeography, vegetation, no continental ice sheets) and the CO_2 concentration forcing on the transport processes are calculated first separately, and then in combination, to allow a full comparison of heat transport in the preindustrial and the early Eocene. The transport processes via the Hadley cell, the monsoon systems and the midlatitude cyclones are analyzed in more detail as these large-scale circulation patterns are identified as being different in the EECO compared to present day.

Our first research question investigates the DeepMIP models' skill in capturing the characteristics of transport processes in the preindustrial simulations (Section 4.1). Overall, the DeepMIP ensemble mean and the reanalysis transport values show good agreement.

The impacts of non-CO_2 constraints (paleogeography, vegetation, no continental ice sheet) on the different transport processes show hemispheric asymmetry. In the $1 \times CO_2$ Eocene simulations the total poleward MHT is smaller in the Northern Hemisphere but larger in the Southern Hemisphere. This is mainly due to the same change in oceanic transport. This shift in oceanic transport toward the South Pole is in line with the strong Southern Hemisphere-driven oceanic overturning circulation of the Eocene, found in the DeepMIP models (Zhang et al., 2022). Considering the different physical processes most notable is the extra heat transport by TE in the midlatitudes, which is compensated by a loss in energy transport via SE. The increase in cyclonic heat transport is explained by changes in paleogeography. The existence of an extra epicontinental sea at the north midlatitudes, with possible high land-sea thermal contrast, results in a semi-permanent pressure system, which impacts the TE at the midlatitudes. Also, the wide Pacific basin results in a split in the Aleutian Low. Thus, in the end during the Eocene boreal winter there were probably 4 semi-permanent low pressure systems present at the northern midlatitudes as opposed to the only two in present day climate. The increase in semi-permanent lows, likely results in an increase in cyclone numbers as well, but to quantify this, one needs high temporal resolution output from the models. A decrease in North Hemispheric monsoon latent heat transport, is also linked to the change in topography, since the location of land areas highly determines the area, where monsoon develops.

Transport changes, which are solely due to CO_2 increases in the 3× and $6 \times CO_2$ EECO simulations, are especially relevant to better understand and predict changes under future climate change. We find that with increasing CO_2 concentrations, the atmosphere transports more heat poleward, while the ocean transports the same amount or less. The results also show that the Hadley cells overturn more heat on the northern side of the Equator, than on the southern side, while their net transport outward of the tropical band is slightly decreasing with CO_2 rise. On the other hand, monsoon systems transport more latent heat from the subtropics to the higher latitudes. This indicates that with CO_2 rise the hydrological cycle intensifies. This agrees well with what have been found in our current changing climate, namely that the global monsoon precipitation shows an increase at the end of the 20th century (Gulev et al., 2021).

Our third research question considers the total change between the PI and EECO simulations, and asks which physical processes are affected the most. In our results we see more changes in the Northern Hemisphere, where the atmosphere transports more heat poleward, while the ocean compensates this with less poleward heat

transport. In the EECO climate, we found an increase in latent heat transport toward the polar regions in both hemispheres' midlatitudes, and a decrease in poleward dry static energy transport, same results as Heinemann et al. (2009). The increase in latent heat transport is connected to the intense polar amplification of the EECO world. From the effected large scale circulation patterns, the Hadley cell changes asymmetrically. In the northern Hadley cell, more energy is being overturned during the EECO climate, than in the present, while the net poleward MOC heat transport stays close to the control simulation. Monsoon systems are also affected by both the non-CO_2 and CO_2 constraint, but in an counteracting way. We found smaller monsoon areas in the Eocene, due to the different topography, but at higher CO_2 concentration the heat transport is more intense due to the warmer atmosphere's higher water holding capacity. This, in the end results in a slightly larger poleward heat transport by the monsoons in the EECO. The midlatitude cyclones' heat transport increase mainly in the Northern Hemisphere, due to the before mentioned topography differences.

In summary, we found that transport processes indicate a more intense hydrological cycle and polar amplification in the warmer EECO compared to the present-day climate. We identified the processes, which are affected by the Eocene boundary conditions and those, which are sensitive to the CO_2 increase. The different boundary conditions cause more southward transport in the ocean, which is only partially compensated by the atmosphere. The Eocene set up increases the heat transport of northern midlatitude cyclones and decreases the global monsoon area. The CO_2 increase, on the other hand causes an increase in poleward atmospheric heat transport. Regarding the large scale circulation patterns, the CO_2 increase results in an increase in the latent heat transport of monsoon systems and more overturning heat in the Hadley circulation, although the net poleward transport of the Hadley cells is not increasing. Nevertheless, there is an asymmetry between the northern and southern Hadley cell, with larger changes in the northern cell. A more detailed analysis of the large scale circulation patterns of the Eocene climate, in higher temporal and spatial resolution model results, and their comparison to proxy data, is the focus of our further research.

Data Availability Statement

The DeepMIP PI and Eocene simulations are available by following the instructions at https://www.deepmip.org/data-eocene/; for more description please see Lunt et al. (2021). Hersbach et al. (2019a, 2019b) was downloaded from the Copernicus Climate Change Service (C3S) Climate Data Store. The scripts to reproduce the figures are available at Kelemen (2023).

References

Anagnostou, E., John, E. H., Babila, T. L., Sexton, P. F., Ridgwell, A., Lunt, D. J., et al. (2020). Proxy evidence for state-dependence of climate sensitivity in the Eocene greenhouse. *Nature Communications*, *11*(1), 4436. https://doi.org/10.1038/s41467-020-17887-x

Barron, E. J. (1987). Eocene equator-to-pole surface ocean temperatures: A significant climate problem? *Paleoceanography*, *2*(6), 729–739. https://doi.org/10.1029/PA002i006p00729

Bjerknes, J. (1964). Atlantic air-sea interaction. *Advances in Geophysics*, *10*, 1–82. https://doi.org/10.1016/S0065-2687(08)60005-9

Brady, E. C., DeConto, R. M., & Thompson, S. L. (1998). Deep water formation and Poleward Ocean heat transport in the warm climate extreme of the Cretaceous (80 Ma). *Geophysical Research Letters*, *25*(22), 4205–4208. https://doi.org/10.1029/1998GL900072

Chan, W.-L., & Abe-Ouchi, A. (2020). Pliocene Model Intercomparison Project (PlioMIP2) simulations using the model for interdisciplinary research on climate (MIROC4m). *Climate of the Past*, *16*(4), 1523–1545. https://doi.org/10.5194/cp-16-1523-2020

Delworth, T. L., Broccoli, A. J., Rosati, A., Stouffer, R. J., Balaji, V., Beesley, J. A., et al. (2006). GFDL's CM2 global coupled climate models. Part I: Formulation and simulation. *Journal of Climate*, *19*(5), 643–674. https://doi.org/10.1175/jcli3629.1

Donohoe, A., Armour, K. C., Roe, G. H., Battisti, D. S., & Hahn, L. (2020). The partitioning of meridional heat transport from the last glacial maximum to CO_2 quadrupling in coupled climate models. *Journal of Climate*, *33*(10), 4141–4165. https://doi.org/10.1175/JCLI-D-19-0797.1

Evans, D., Sagoo, N., Renema, W., Cotton, L. J., Müller, W., Todd, J. A., et al. (2018). Eocene greenhouse climate revealed by coupled clumped isotope-Mg/Ca thermometry. *Proceedings of the National Academy of Sciences of the United States of America*, *115*(6), 1174–1179. https://doi.org/10.1073/pnas.1714744115

Forster, P., Storelvmo, T., Armour, K., Collins, W., Dufresne, J.-L., Frame, D., et al. (2021). Earth's energy budget, climate feedbacks, and climate sensitivity. In V. Masson-Delmotte, P. Zhai, A. Pirani, S. L. Connors, C. Péan, S. Berger, et al. (Eds.), *Climate change 2021: The physical science basis. Contribution of working group I to the sixth assessment report of the intergovernmental panel on climate change* (pp. 923–1054). Cambridge University Press. https://doi.org/10.12006/j.issn.1673-1719.2021.191

Gulev, S. K., Thorne, P. W., Ahn, J., Dentener, F. J., Domingues, C. M., Gerland, S., et al. (2021). Changing state of the climate system. In V. Masson-Delmotte, P. Zhai, A. Pirani, S. L. Connors, C. Péan, S. Berger, et al. (Eds.), *Climate change 2021: The physical science basis. Contribution of working group I to the sixth assessment report of the intergovernmental panel on climate change* (pp. 287–422). Cambridge University Press. https://doi.org/10.1017/9781009157896.004.288

Hasumi, H. (2000). CCSR Ocean Component model (COCO) version 2.1, technical report.

Heinemann, M., Jungclaus, J. H., & Marotzke, J. (2009). Warm Paleocene/Eocene climate as simulated in ECHAM5/MPI-OM. *Climate of the Past*, *5*(4), 785–802. https://doi.org/10.5194/cp-5-785-2009

Held, I. M. (2001). The partitioning of the poleward energy transport between the tropical ocean and atmosphere. *Journal of the Atmospheric Sciences*, *58*(8), 943–948. https://doi.org/10.1175/1520-0469(2001)058<0943:TPOTPE>2.0.CO;2

Herold, N., Buzan, J., Seton, M., Goldner, A., Green, J. A. M., Müller, R. D., et al. (2014). A suite of early Eocene (∼55 Ma) climate model boundary conditions. *Geoscientific Model Development*, *7*(5), 2077–2090. https://doi.org/10.5194/gmd-7-2077-2014

Hersbach, H., Bell, B., Berrisford, P., Biavati, G., Horányi, A., Muñoz Sabater, J., et al. (2019a). ERA5 monthly averaged data on pressure levels from 1959 to present [Dataset]. Copernicus Climate Change Service (C3S) Climate Data Store (CDS). https://doi.org/10.24381/cds.6860a573

Hersbach, H., Bell, B., Berrisford, P., Biavati, G., Horányi, A., Muñoz Sabater, J., et al. (2019b). ERA5 monthly averaged data on single levels from 1959 to present [Dataset]. Copernicus Climate Change Service (C3S) Climate Data Store (CDS). https://doi.org/10.24381/cds.f17050d7

Hersbach, H., Bell, B., Berrisford, P., Hirahara, S., Horányi, A., Muñoz-Sabater, J., et al. (2020). The ERA5 global reanalysis. *Quarterly Journal of the Royal Meteorological Society*, *146*(730), 1999–2049. https://doi.org/10.1002/qj.3803

Hollis, C. J., Dunkley Jones, T., Anagnostou, E., Bijl, P. K., Cramwinckel, M. J., Cui, Y., et al. (2019). The DeepMIP contribution to PMIP4: Methodologies for selection, compilation and analysis of latest Paleocene and early Eocene climate proxy data, incorporating version 0.1 of the DeepMIP database. *Geoscientific Model Development*, *12*(7), 3149–3206. https://doi.org/10.5194/gmd-12-3149-2019

Huber, M., & Nof, D. (2006). The ocean circulation in the southern hemisphere and its climatic impacts in the Eocene. *Palaeogeography, Palaeoclimatology, Palaeoecology*, *231*(1–2), 9–28. https://doi.org/10.1016/j.palaeo.2005.07.037

Huber, M., & Sloan, L. C. (2001). Heat transport, deep waters, and thermal gradients: Coupled simulation of an Eocene greenhouse climate. *Geophysical Research Letters*, *28*(18), 3481–3484. https://doi.org/10.1029/2001GL012943

Hurrell, J. W., Holland, M. M., Gent, P. R., Ghan, S., Kay, J. E., Kushner, P. J., et al. (2013). The community earth system model: A framework for collaborative research. *Bulletin of the American Meteorological Society*, *94*(9), 1339–1360. https://doi.org/10.1175/BAMS-D-12-00121.1

Hutchinson, D. K., Coxall, H. K., O'Regan, M., Nilsson, J., Caballero, R., & de Boer, A. M. (2019). Arctic closure as a trigger for Atlantic overturning at the Eocene-Oligocene transition. *Nature Communications*, *10*(1), 3797. https://doi.org/10.1038/s41467-019-11828-z

Hutchinson, D. K., De Boer, A. M., Coxall, H. K., Caballero, R., Nilsson, J., & Baatsen, M. (2018). Climate sensitivity and meridional overturning circulation in the late Eocene using GFDL CM2.1. *Climate of the Past*, *14*(6), 789–810. https://doi.org/10.5194/cp-14-789-2018

Inglis, G. N., Bragg, F., Burls, N., Evans, D., Foster, G., Huber, M., et al. (2020). Global mean surface temperature and climate sensitivity of the EECO, PETM and latest Paleocene. *Climate of the Past Discussions*, *44*(January), 1–43. https://doi.org/10.31223/osf.io/8527z

IPCC. (2021). Annex V: Monsoons [Cherchi, A., A. Turner (eds.)]. In V. Masson-Delmotte, P. Zhai, A. Pirani, S. L. Connors, C. Péan, S. Berger, et al. (Eds.), *Climate change 2021: The physical science basis. Contribution of working group I to the sixth assessment report of the intergovernmental panel on climate change* (pp. 2193–2204). Cambridge University Press. https://doi.org/10.1017/9781009157896.019.2193

Kelemen, F. D. (2023). Meridional Heat Transport in the DeepMIP Eocene ensemble, scripts for figures in Kelemen et al. (2023) [Software]. Zenodo. https://doi.org/10.5281/zenodo.7958397

Kiehl, J. T., & Shields, C. A. (2013). Sensitivity of the palaeocene-eocene thermal maximum climate to cloud properties. *Philosophical Transactions of the Royal Society A: Mathematical, Physical & Engineering Sciences*, *371*(2001), 20130093. https://doi.org/10.1098/rsta.2013.0093

Kitoh, A., Endo, H., Krishna Kumar, K., Cavalcanti, I. F. A., Goswami, P., & Zhou, T. (2013). Monsoons in a changing world: A regional perspective in a global context. *Journal of Geophysical Research: Atmospheres*, *118*(8), 3053–3065. https://doi.org/10.1002/jgrd.50258

Krapp, M., & Jungclaus, J. H. (2011). The Middle Miocene climate as modelled in an atmosphere-ocean-biosphere model. *Climate of the Past*, *7*(4), 1169–1188. https://doi.org/10.5194/cp-7-1169-2011

Lee, J.-Y., Marotzke, J., Bala, G., Cao, L., Corti, S., Dunne, J. P., et al. (2021). Future global climate: Scenario-based projections and near-term information. In *Climate change 2021: The physical science basis. Contribution of working group I to the sixth assessment report of the intergovernmental panel on climate change*. https://doi.org/10.1017/9781009157896.006.553

Licht, A., Van Cappelle, M., Abels, H. A., Ladant, J. B., Trabucho-Alexandre, J., France-Lanord, C., et al. (2014). Asian monsoons in a late Eocene greenhouse world. *Nature*, *513*(7519), 501–506. https://doi.org/10.1038/nature13704

Lunt, D. J., Bragg, F., Chan, W.-L., Hutchinson, D. K., Ladant, J. B., Morozova, P., et al. (2021). DeepMIP: Model intercomparison of early Eocene climatic optimum (EECO) large-scale climate features and comparison with proxy data. *Climate of the Past*, *17*(1), 203–227. https://doi.org/10.5194/cp-17-203-2021

Lunt, D. J., Huber, M., Anagnostou, E., Baatsen, M. L. J., Caballero, R., DeConto, R., et al. (2017). The DeepMIP contribution to PMIP4: Experimental design for model simulations of the EECO, PETM, and pre-PETM (version 1.0). *Geoscientific Model Development*, *10*(2), 889–901. https://doi.org/10.5194/gmd-10-889-2017

Lunt, D. J., Jones, T. D., Heinemann, M., Huber, M., LeGrande, A., Winguth, A., et al. (2012). A model-data comparison for a multi-model ensemble of early Eocene atmosphere-ocean simulations: EoMIP. *Climate of the Past*, *8*(5), 1717–1736. https://doi.org/10.5194/cp-8-1717-2012

Marshall, J., Donohoe, A., Ferreira, D., & McGee, D. (2014). The ocean's role in setting the mean position of the Inter-Tropical Convergence Zone. *Climate Dynamics*, *42*(7–8), 1967–1979. https://doi.org/10.1007/s00382-013-1767-z

Marsland, S. J., Haak, H., Jungclaus, J. H., Latif, M., & Röske, F. (2003). The Max-Planck-Institute global ocean/sea ice model with orthogonal curvilinear coordinates. *Ocean Modelling*, *5*(2), 91–127. https://doi.org/10.1016/S1463-5003(02)00015-X

Masuda, K. (1988). Meridional heat transport by the atmosphere and the ocean: Analysis of FGGE data. *Tellus, Series A*, *40A*(4), 285–302. https://doi.org/10.3402/tellusa.v40i4.11801

Outten, S., Esau, I., & Otterå, O. H. (2018). Bjerknes compensation in the CMIP5 climate models. *Journal of Climate*, *31*(21), 8745–8760. https://doi.org/10.1175/JCLI-D-18-0058.1

Roeckner, E., Bäuml, G., Bonaventura, L., Brokopf, R., Esch, M., Giorgetta, M., et al. (2003). The atmospheric general circulation model ECHAM 5. PART I: Model description (Issue 140).

Salzmann, M. (2017). The polar amplification asymmetry: Role of Antarctic surface height. *Earth System Dynamics*, *8*(2), 323–336. https://doi.org/10.5194/esd-8-323-2017

Sarkar, S., Basak, C., Frank, M., Berndt, C., Huuse, M., Badhani, S., & Bialas, J. (2019). Late Eocene onset of the proto-Antarctic circumpolar current. *Scientific Reports*, *9*(1), 10125. https://doi.org/10.1038/s41598-019-46253-1

Sloan, L. C., Walker, J. C. G., & Moore, T. C., Jr. (1995). Possible role of oceanic heat transport in Early Eocene climate. *Paleoceanography*, *10*(2), 347–356. https://doi.org/10.1029/94PA02928

Smith, R. S., Dubois, C., & Marotzke, J. (2006). Global climate and ocean circulation on an aquaplanet ocean-atmosphere general circulation model. *Journal of Climate*, *19*(18), 4719–4737. https://doi.org/10.1175/JCLI3874.1

Stepanek, C., & Lohmann, G. (2012). Modelling mid-Pliocene climate with COSMOS. *Geoscientific Model Development*, *5*(5), 1221–1243. https://doi.org/10.5194/gmd-5-1221-2012

Stone, P. H. (1978). Constraints on dynamical transports of energy on a spherical planet. *Dynamics of Atmospheres and Oceans*, *2*, 123–139. https://doi.org/10.1016/0377-0265(78)90006-4

Takata, K., Emori, S., & Watanabe, T. (2003). Development of the minimal advanced treatments of surface interaction and runoff. *Global and Planetary Change*, *38*(1–2), 209–222. https://doi.org/10.1016/S0921-8181(03)00030-4

Tang, H., Eronen, J. T., Micheels, A., & Ahrens, B. (2013). Strong interannual variation of the Indian summer monsoon in the Late Miocene. *Climate Dynamics*, *41*(1), 135–153. https://doi.org/10.1007/s00382-012-1655-y

Valdes, P. J., Armstrong, E., Badger, M. P. S., Bradshaw, C. D., Bragg, F., Crucifix, M., et al. (2017). The BRIDGE HadCM3 family of climate models: HadCM3@Bristol v1.0. *Geoscientific Model Development*, *10*(10), 3715–3743. https://doi.org/10.5194/gmd-10-3715-2017

Wang, B., & Ding, Q. (2008). Global monsoon: Dominant mode of annual variation in the tropics. *Dynamics of Atmospheres and Oceans*, *44*(3–4), 165–183. https://doi.org/10.1016/j.dynatmoce.2007.05.002

Watt-Meyer, O., Frierson, D. M. W., & Fu, Q. (2019). Hemispheric asymmetry of tropical expansion under CO_2 forcing. *Geophysical Research Letters*, *46*(15), 9231–9240. https://doi.org/10.1029/2019GL083695

Wills, R. C. J., White, R. H., & Levine, X. J. (2019). Northern hemisphere stationary waves in a changing climate. *Current Climate Change Reports*, *5*(4), 372–389. https://doi.org/10.1007/s40641-019-00147-6

Xian, T., Xia, J., Wei, W., Zhang, Z., Wang, R., Wang, L. P., & Ma, Y. F. (2021). Is Hadley cell expanding? *Atmosphere*, *12*(12), 1–31. https://doi.org/10.3390/atmos12121699

Yang, H., Zhao, Y., Liu, Z., Li, Q., He, F., & Zhang, Q. (2015). Heat transport compensation in atmosphere and ocean over the past 22,000 years. *Scientific Reports*, *5*, 1–11. https://doi.org/10.1038/srep16661

Zhang, Y., de Boer, A. M., Lunt, D. J., Hutchinson, D. K., Ross, P., van de Flierdt, T., et al. (2022). Early Eocene ocean meridional overturning circulation: The roles of atmospheric forcing and strait geometry. *Paleoceanography and Paleoclimatology*, *37*(3), 1–22. https://doi.org/10.1029/2021PA004329